




Article

Growth and Performance of Perovskite Semiconductor CsPbX₃ (X = Cl, Br, I, or Mixed Halide) for Detection and Imaging Applications

R. Hawrami ^{1,*}, L. Matei ¹, E. Ariesanti ¹, V. Buliga ¹, H. Parkhe ¹, A. Burger ¹, J. Stewart ¹, A. Piro ¹, F. De Figueiredo ¹ , A. Kargar ², K. S. Bayikadi ³, J. Reiss ⁴  and D. E. Wolfe ⁴ 

¹ Department of Life and Physical Sciences, Physics Division, Fisk University, 1000 17th Avenue N, Nashville, TN 37208, USA

² Radiation Monitoring Devices, Inc., 44 Hunt Street, Watertown, MA 02472, USA

³ Department of Chemistry, Northwestern University, 2145 Sheridan Road, Evanston, IL 60208, USA

⁴ Department of Materials Science and Engineering, Pennsylvania State University, University Park, PA 16802, USA

* Correspondence: rhawrami@fisk.edu

Abstract: The material family halide perovskites has been critical in recent room-temperature radiation detection semiconductor research. Cesium lead bromide (CsPbBr₃) is a halide perovskite that exhibits characteristics of a semiconductor that would be suitable for applications in various fields. In this paper, we report on the correlations between material purification and crystal material properties. Crystal boules of CsPbX₃ (where X = Cl, Br, I, or mixed) were grown with the Bridgman growth method. We describe in great detail the fabrication techniques used to prepare sample surfaces for contact deposition and sample testing. Current–voltage measurements, UV–Vis and photocurrent spectroscopy, as well as photoluminescence measurements, were carried out for material characterization. Bulk resistivity values of up to $3.0 \times 10^9 \Omega \cdot \text{cm}$ and surface resistivity values of $1.3 \times 10^{11} \Omega / \square$ indicate that the material can be used for low-noise semiconductor detector applications. Preliminary radiation detectors were fabricated, and using photocurrent measurements we have estimated a value of the mobility–lifetime product for holes $(\mu\tau)_h$ of $2.8 \times 10^{-5} \text{ cm}^2/\text{V}$. The results from the sample testing can shed light on ways to improve the crystal properties for future work, not only for CsPbX₃ but also other halide perovskites.

Keywords: cesium lead halide perovskite; bulk single crystal growth; melt growth; room temperature semiconductor detector



Citation: Hawrami, R.; Matei, L.; Ariesanti, E.; Buliga, V.; Parkhe, H.; Burger, A.; Stewart, J.; Piro, A.; De Figueiredo, F.; Kargar, A.; et al. Growth and Performance of Perovskite Semiconductor CsPbX₃ (X = Cl, Br, I, or Mixed Halide) for Detection and Imaging Applications. *Materials* **2024**, *17*, 5360. <https://doi.org/10.3390/ma17215360>

Academic Editors: Abderrahim Yassar and Albena Paskaleva

Received: 18 September 2024

Revised: 24 October 2024

Accepted: 30 October 2024

Published: 1 November 2024



Copyright: © 2024 by the authors. Licensee MDPI, Basel, Switzerland. This article is an open access article distributed under the terms and conditions of the Creative Commons Attribution (CC BY) license (<https://creativecommons.org/licenses/by/4.0/>).

1. Introduction

Finding the next room-temperature semiconductor detector that will transform the future of radiation detection technology has been the pursuit of many researchers around the world. The growing interest in room-temperature radiation detectors has led to an extensive effort to develop new materials, both scintillators and semiconductors, that address specific challenges of various applications in the fields of homeland security (nonproliferation of nuclear materials) and industrial and medical imaging, as well as fundamental scientific research [1–3]. Compared to scintillators, which have the intrinsic non-proportionality of the light yield and the obvious need of a photosensor to convert the light into electrical signal, semiconductor radiation detectors present the advantage of direct conversion characteristics while providing a superior spectroscopic performance [4,5]. Semiconductors can be easily integrated in front-end electronics systems to achieve a better performance in terms of energy resolution and spatial resolution, if pixelated contacts are used [6].

There has been extensive research conducted for room-temperature radiation detection semiconductors. Cadmium zinc telluride (CZT) is a room-temperature semiconductor

detector which has been substantially researched over the last thirty years. Because CZT is sensitive to a wide range of photon energy, it can be used in many applications. The Bridgman melt growth method has been the main method to produce CZT crystal ingots. This growth method, however, causes many crystalline defects such as twinning, stacking faults, grain boundaries, and zinc segregation [7]. Phase defects are another limitation observed when growing CZT. While CZT has excellent charge properties, these growth and material issues have prevented the widespread use of CZT as a room-temperature detector due to availability and production cost.

Another promising radiation detector material is thallium bromide (TlBr), which has been hailed as the next promising material among wide bandgap semiconductor materials to rival CZT [8]. The high stopping power of its elements ($Z_{\text{eff}} = 58$) and density (7.56 g/cm^3) make it suitable for many applications in astrophysics, medicine, and military applications [8]. However, TlBr is soft and current material quality limits its gamma ray detection capabilities [8]. Both of these properties make TlBr difficult to develop for widespread use.

Cesium lead bromide CsPbBr_3 (CPB) is the latest promising room-temperature semiconductor detector that has been the focus of recent research [9–16]. It falls into the halide perovskite family of materials that follows an ABX_3 crystal structure. CPB is a promising semiconductor crystal in that it has optoelectronic properties characterized by a high carrier mobility, as well as a large bandgap (2.25 eV) which offers the possibility of low noise performance at room temperature. The all-inorganic perovskite CPB, with its wide band and broad valence and conduction bands, can be grown in a large size both from melt and from solution [9,10,15,16]. CPB has a high effective atomic number, Z_{eff} , of 65.9, which is higher than CZT ($Z_{\text{eff}} = 50.2$), leading to higher photon stopping power especially in the high-energy region ($>500 \text{ keV}$). The quality of the grown material can be improved by including a zone-refining step after material synthesis, which resulted in a higher purity material being grown. The grown crystal demonstrated the capability to detect alpha particles and gamma radiation. The use of asymmetric contacts on the wafers of CsPbBr_3 proved to optimize the leakage currents and improve the detection capabilities [11–14].

In this paper, the growth and the characterization of CPB crystals at Fisk University (Fisk) is described. Pre-growth material purification by zone-refining was conducted in-house, which resulted in pre-cursor materials with a purity of 99.999%. The purified materials were used to grow single bulk CPB ingots by the Bridgman method. While the growth optimization of CPB is the main factor that improves material properties, different fabrication techniques, such as etching with different bromine concentration and different immersion times, also have the potential to improve detector performance. CPB meets most of the requirements for X-ray and gamma ray detection with fewer limitations compared to other room-temperature radiation detector materials.

2. Experimental Methods

2.1. Material Purification and Crystal Growth

Crystals with a low defect density are crucial for semiconductor spectrometer performance. Such crystals are usually grown with $>5 \text{ N}$ precursor materials. The raw starting materials CsX and PbX_2 ($X = \text{Cl, Br, I}$) with 4–5 N purity levels were ordered from different chemical vendors. The growth process was started by synthesizing CsPbX_3 with the as-received materials. The synthesized material was then used as a charge for initial growth runs. Purification of the synthesized charge was carried out when the purity level was considered not acceptable, based on the crystal color or appearance, material analysis using a differential scanning calorimeter, and the device performance. The zone-refining technique [17] was used for the purification of each binary compound CsX and PbX_2 , as well as the synthesized CsPbX_3 compounds, respectively. Figure 1a shows the zone-refining system and ampoule used to purify CsPbBr_3 . Figure 1b shows the CsPbBr_3 materials synthesized from the materials as received from the vendors, showing the inclusion of possible carbonaceous or organics impurities. Figure 1c shows the cleaned CsPbBr_3 that

was subsequently used as the charge for the zone-refining process. Figure 1d shows the zone-refined CsPbBr₃ material that was then used as the growth charge. Material colors observed as seen in Figure 1b–d can be a visual indicator to the quality of the starting growth materials for CsPbBr₃.

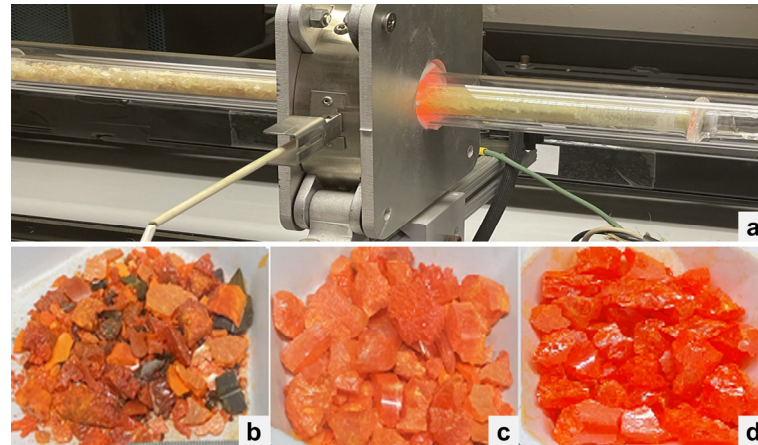


Figure 1. (a) Purification of CsPbBr₃ with a zone-refining system at Fisk. (b) CsPbBr₃ synthesized from the as-received materials. (c) Cleaned CsPbBr₃ synthesized materials. (d) Zone-refined CsPbBr₃ materials.

The Bridgman method [18] was used to grow bulk CsPbX₃ single crystal ingots at Fisk. The purified materials were loaded into a clean quartz ampoule inside an inert atmosphere glove box to grow 15 mm through 51 mm diameter bulk ingots. The ampoule was then attached to a vacuum-heater system, dehydrated, and sealed under high vacuum. The sealed ampoule was loaded into a two-zone vertical furnace with a growth speed of 3.5 mm/h. After crystallization, the furnace was cooled down to room temperature at a rate of 100–150 °C/day. Figure 2a shows an as-grown 16 mm diameter CsPbCl₃ crystal boule grown with zone-refined starting materials, while Figure 2b shows an as-grown 1-inch diameter CsPbCl₃ crystal boule grown with non-purified materials. Figure 2c show a 1-inch diameter CsPbBr₃ crystal boule grown with non-purified materials, while Figure 2d show a 1-inch diameter CsPbBr₃ crystal boule grown with purified materials. As seen in Figure 2a–d, the CsPbX₃ ingots grown with purified materials were clear and transparent (Figure 2a,d) compared to the ones grown with non-purified materials (Figure 2b,c).

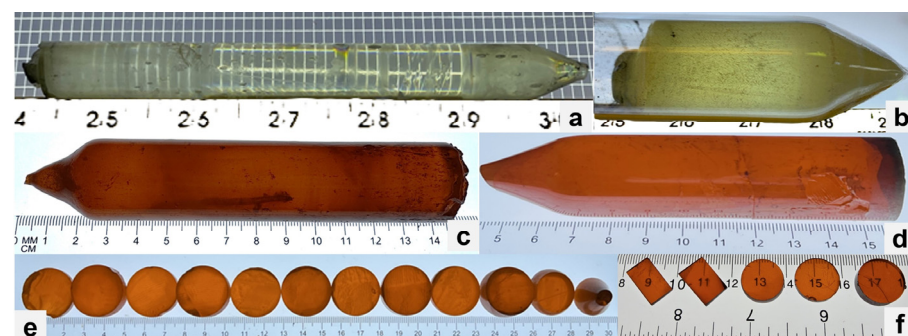


Figure 2. (a) CsPbCl₃ grown with purified materials. (b) CsPbCl₃ grown with non-purified materials. (c) CsPbBr₃ grown with non-purified materials. (d) CsPbBr₃ grown with purified materials. (e) CsPbBr₃ wafers cut transversely. (f) CsPbBr₃ samples cut longitudinally and transversely.

2.2. Crystal Processing, Detector Fabrication, and Characterization Methods

After growth, the crystal boule was removed from the ampoule and then cut with a diamond wire saw. The crystal boule was cut either longitudinally (along the axis of the

boule) or transversely (crosswise). Figure 2e shows CsPbBr₃ crystal samples cut transversely off the boule, while Figure 2f shows rectangular crystal samples cut longitudinally (along the boule) and circular platelet samples from the boule cut transversely. The cut samples were then lapped (roughly polished) and finely polished with Al₂O₃ or SiC polishing papers. Prior to contact deposition, samples were cleaned for less than 10 s in hexane and dried with lint-free wipes. Metal contacts were deposited using RF sputtering. The polished crystals and fabricated devices underwent characterization by several methods. Optical microscope was used to determine cutting direction and crystal quality. Transmission/absorption measurements of polished crystal samples were performed using Agilent Cary 4000 UV–VIS. Current–voltage (I–V) measurements were conducted using a test box fabricated in-house (Figure 3) and a Keithley 237 High Voltage Source Meter unit. Photocurrent spectroscopy was carried out using the same test box now covered by a lid with an aperture to allow light from an Oriel (Newport) 100 W quartz tungsten halogen lamp to reach the sample. Monochromatic light was produced using an Oriel (Newport) C130 monochromator, with the wavelength varied from 200 to 1000 nm in steps of 5 nm. During this variation, the voltage across the sample was maintained at a constant bias. The mobility–lifetime ($\mu\tau$) product was estimated using photocurrent spectroscopy and alpha particle spectroscopy.

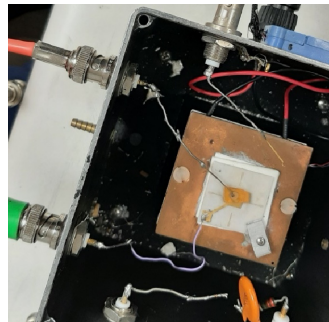


Figure 3. The test box for I–V characteristics.

Several CsPbX₃ crystal samples were sent to several collaborators as bare crystals or with metal contacts. At RMD, Inc. (RMD), CsPbBr₃ samples (one of them is shown in Figure 4a, with a thickness of 2.1 mm) were fabricated with approximately 600 Å gold (Au) contacts on one side of the samples, while eutectic gallium–indium (GaIn) was used on the opposite side to form rectifying contacts. Carbon paste was used to attach 2-mm palladium (Pd) wires to the Au contacts. Samples were then mounted on glass substrates for characterization. One of the fabricated planar detectors is shown in Figure 4b with the Au contacts facing up. On the fabricated devices, two main measurements were employed for characterization purposes: current–voltage (I–V) measurements and radiation measurements (gamma rays). The planar CsPbBr₃ detectors were first characterized for current–voltage (I–V) characteristic measurement using a pico-amp meter. Since the mobility–lifetime product of holes is known to be higher than electrons in CsPbBr₃ [9], the reading electrode should be sensing the holes; therefore, the reading Au contact was grounded (through the preamplifier) and the GaIn contact was positively biased. The wired detector was secured on a glass substrate using Kapton tapes with the Au contact facing up. An aluminum test box was used to test the CsPbBr₃ planar device for the radiation response. A high-voltage power supply, Cremat CR-110 preamplifier, shaping amplifier, and multi-channel analyzer, and a Tail Pulse Generator (TPG) were used to acquire pulse height spectra. Northwestern University (Northwestern) received a CsPbBr₃ sample that was fabricated into a device shown in Figure 4c with a 300 nm In as the anode and 150 nm platinum (Pt) as the cathode. Northwestern also received a CsPb(Br,I)₃ sample (Figure 4d), which was fabricated into a device with a 600 nm sputtered lead (Pb) as the anode and 150 nm evaporated Au as the cathode (Figure 4e).

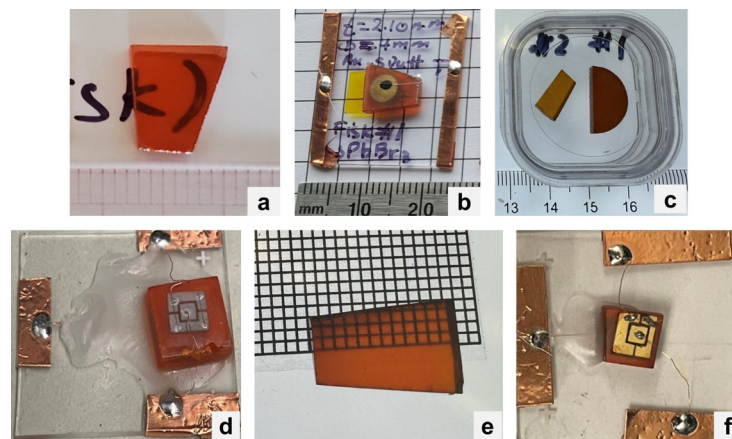


Figure 4. (a) CsPbBr₃ sample sent to RMD. (b) Planar device fabricated from the sample in (a). (c) CsPbBr₃ samples sent to Penn State. (d) CsPbBr₃ sample fabricated into a device at Northwestern. (e) CsPb(Br,I)₃ sample sent to Northwestern. (f) CsPb(Br,I)₃ device fabricated from the sample in (e).

Pennsylvania State University (Penn State) received two CsPbBr₃ samples: one was cut from the boule crosswise (perpendicular to the growth direction) and one cut from the boule longitudinally (parallel to the growth direction). Surface preparation methods need to be developed in order to obtain ultra-smooth, nm-level surface roughness as it enables reduced surface defect concentration, improved charge transport between the semiconductor and electrode, and overall increased sample reproducibility. Recent literature reports suggest that chemical–mechanical polishing (CMP) approaches may be viable for the CsPbBr₃ crystal system [19]. This approach was adapted at Penn State and implemented on the CsPbBr₃ crystals received from Fisk. CsPbBr₃ crystals were first polished using 800 and 1200 grit SiC paper, followed by a 1 μm polishing suspension on a neoprene polishing pad. Chemical–mechanical polishing was then performed to eliminate further scratching. Crystals were mechanically abraded using the neoprene polishing pad and a chemical etchant lubricant comprised of isopropyl alcohol and dimethylsulfoxide (DMSO) suspension (50/50 vol%). Figure 5 shows optical micrographs of the CsPbBr₃ crystal surface after each step of the polishing process. The CMP process clearly eliminates all major scratches from the surface, leaving behind only some residual minor scratch marks. Critically, this process also only takes 30 s and can be applied more uniformly across sample sets.

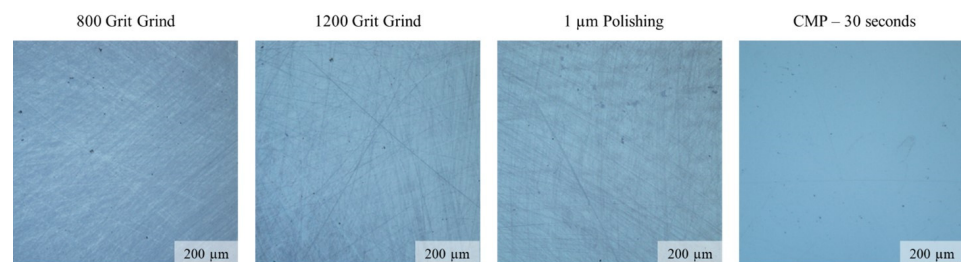


Figure 5. Optical microscopy of a single CsPbBr₃ crystal taken at each stage of the polishing process. The CMP step significantly reduces observed scratching across the surface of the crystal.

Crystals were then dried with nitrogen and placed into storage in vacuum and in the dark. Passivation was performed using a Plasma-Enhanced Atomic Layer Deposition (PE-ALD) system. In total, 10 nm of SiO₂ was deposited using a tris(dimethylamino)silane (TDMAS, 99+%) precursor source, with alternating static dose cycles with 400 W O₂ plasma. To finalize the device fabrication, 50 nm-thick titanium and gold electrodes were deposited via electron-beam physical vapor deposition (EB-PVD). X-ray Diffraction (XRD) was performed on across a 2θ range of 20–80 °C (0.01°/step, 2.5 s/step) using

Bragg–Brentano geometry. The operating voltage (40 kV), current (45 mA), and source (Cu, 1.5406 Å) were held constant during all measurements. Phase identification and peak fitting was performed using JADE software. Electrical measurements were conducted with a Keithly 4200 source meter under ambient conditions.

3. Results and Analysis

3.1. I–V Characteristics and Gamma-Ray Measurements

Figure 6a shows a 3 mm-thick CsPbBr₃ processed sample with three sputtered metal contacts with different diameters: Ø 1 mm, Ø 2 mm, and Ø 4 mm. For this planar device, Au and Bi contacts were deposited using RF sputtering on opposite parallel faces. The sample was placed on a thermo-regulated stage maintained at 20 °C for the duration of the measurements. Variable forward and reverse biases were applied using a source meter and the current was measured for each voltage.

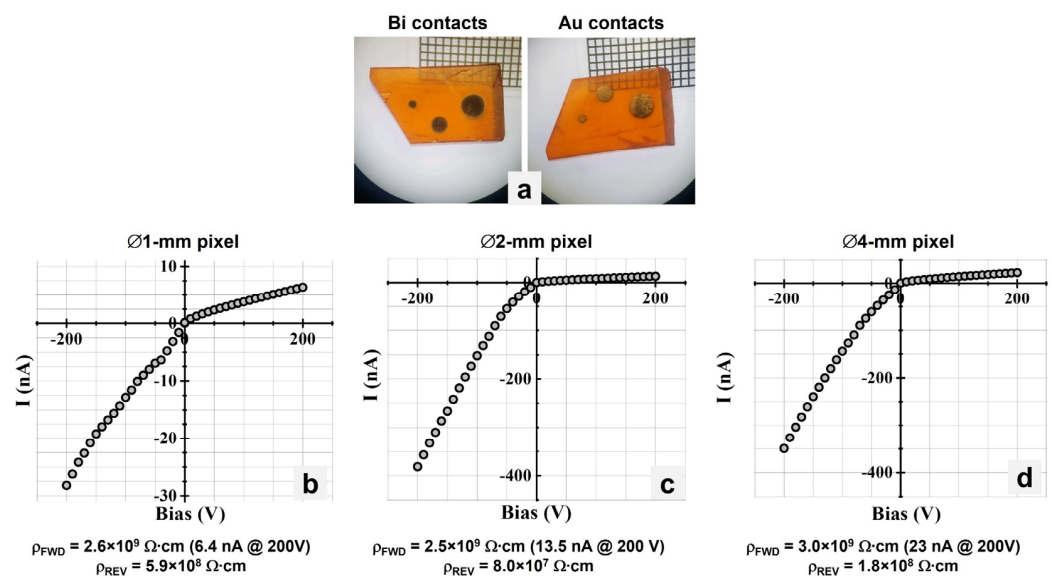


Figure 6. (a) CsPbBr₃ sample with differently sized contacts. (b) I–V characteristics for Ø 1 mm contacts. (c) I–V characteristics for Ø 2 mm contacts. (d) I–V characteristics for Ø 4 mm contacts.

The resistivity was determined using linear least squares fitting (with the formula $y = a + bx$, where x is the applied bias (in V), y is the measured current (in Å), a is a constant, and b is the slope of the line fit) on the I–V characteristics data. The slope of the line fit is the calculated inverse resistance R^{-1} (in Ω^{-1}). The resistivity ρ (in $\Omega \cdot \text{cm}$) is found using the following relationship:

$$R = \rho \frac{L}{A} \quad (1)$$

where L is the sample thickness (in cm) and A is the contact area (in cm²). Figure 6b–d show the I–V characteristic graphs for the differently sized contacts that exhibit rectifying behavior. The bulk resistivity values ranged from 2.2×10^9 to 3.0×10^9 $\Omega \cdot \text{cm}$ for forward bias (FWD) and 8.0×10^7 to 5.9×10^8 $\Omega \cdot \text{cm}$ for reverse bias (REV). Leakage currents at 6.4 nA, 13.5 nA, and 23 nA were measured at +200 V for Ø 1 mm, Ø 2 mm, and Ø 4 mm contacts, respectively.

Figure 7a shows a 2 mm-thick CsPbBr₃ sample fabricated with a Au–CsPbBr₃–Au planar device configuration (Ø 4 mm Au contacts and an Au guard ring with an inner diameter of 5 mm) to determine the bulk and surface resistivities. Figure 7b shows the I–V characteristics to determine the bulk resistivity, while Figure 7c shows the I–V characteristics to determine the surface resistivity. Using Equation (1), the bulk resistivity was calculated to be 9.5×10^8 $\Omega \cdot \text{cm}$ for the forward bias (up to +5 V) and 2.8×10^9 $\Omega \cdot \text{cm}$ for the reverse

bias. A leakage current of 1.2 nA was measured at -10 V. The surface resistivity ρ_S (in Ω/sq) was calculated using the following formula:

$$\rho_S = R_S \frac{2\pi}{\ln\left(\frac{R_2}{R_1}\right)} \quad (2)$$

where R_S is the surface resistance (in Ω , calculated from the line fit of the I–V characteristics), R_1 (in mm) is the radius of the metal contact, and R_2 (in mm) is the inner diameter of the guard ring. Using Equation (2), the surface resistivity was calculated to be $2.9 \times 10^{10} \Omega/\text{sq}$ for the forward bias (up to $+4.5$ V) and $1.3 \times 10^{11} \Omega/\text{sq}$ for the reverse bias.

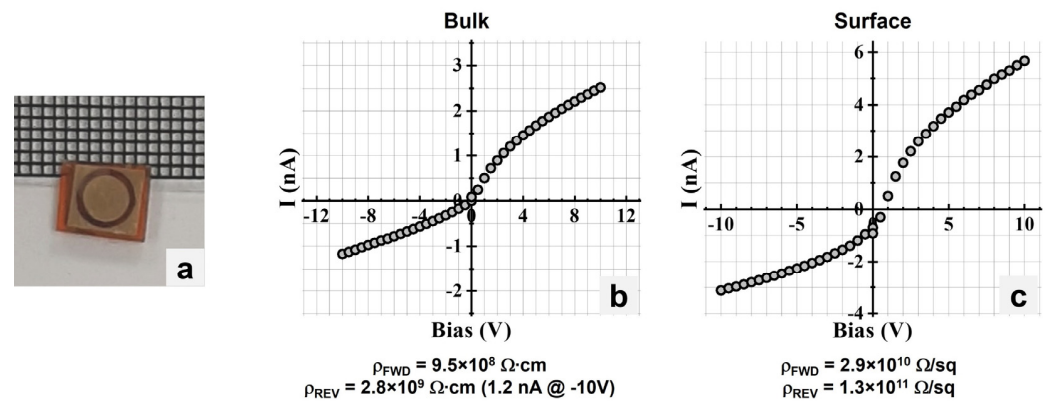


Figure 7. (a) CsPbBr₃ sample with Au–Au contacts and Au guard ring. (b) I–V characteristics to determine bulk resistivity. (c) I–V characteristics to determine surface resistivity.

Figure 8a shows the I–V characteristics for the CsPbBr₃ planar device fabricated at RMD (inset picture and Figure 4b). The device showed an effective resistivity of $2 \times 10^9 \Omega\text{-cm}$ for the forward bias and a leakage current of 51 nA at $+200$ V. Note that due to the different metals being used to form the contacts, a rectifying behavior was observed for the device. Figure 8b shows the background (no source) and ⁶⁰Co spectra collected by the CsPbBr₃ planar device after two days of conditioning process. The conditioning process refers to a process in which a continuous voltage is applied to a detector for a period of time to improve the device performance. For this measurement, the NIM shaping amplifier was set to a gain of 100 and a shaping time of 6 μs , and the device was irradiated from the top Au contact using a ⁶⁰Co source. The device was initially biased at 50 V for the first day and the bias was increased to 100 V for the second day. The device was unstable and noisy within the first day of conditioning at $+50$ V and continued to become more stable with time under bias; however, it became noisier and more unstable after the fourth day. Despite the noise level, the leakage current remained acceptably low and stable.

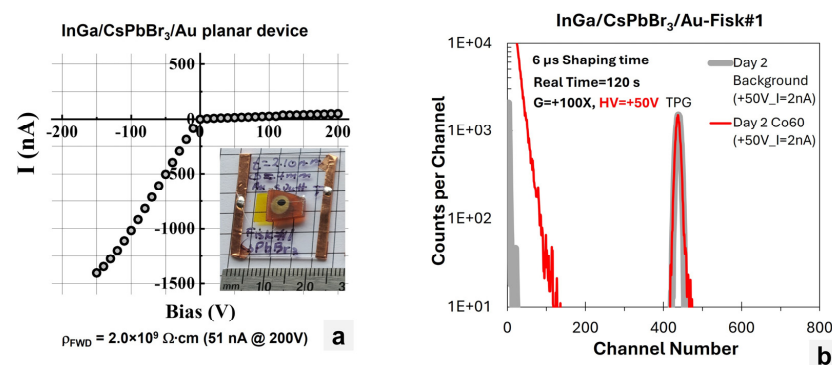


Figure 8. (a) I–V characteristics of InGa–CsPbBr₃–Au planar device (inset) fabricated at RMD. (b) Background and ⁶⁰Co spectra collected by the planar device.

Figure 9a,b show the I–V characteristics for the CsPbBr₃ and CsPb(Br,I)₃ planar devices, both fabricated at Northwestern (Figure 4c,e). The In–CsPbBr₃–Pt exhibited a rectifying behavior with a breakdown voltage around –400 V, while the Pb–CsPb(Br,I)₃–Au device exhibited a resistive behavior. Similar to the devices fabricated at RMD, the CsPbBr₃ device fabricated at Northwestern was very noisy; however, the leakage or dark current remained low.

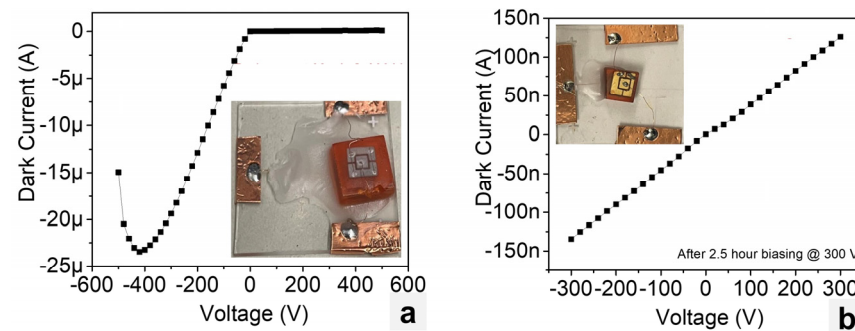


Figure 9. The I–V characteristics for planar devices fabricated at Northwestern: (a) In–CsPbBr₃–Pt and (b) Pb–CsPb(Br,I)₃–Au.

Figure 10 shows the I–V characteristics of the fabricated CsPbBr₃ devices with crystals cut perpendicular and parallel to the growth direction. The perpendicular sample clearly shows an I–V characteristic matching that of a rectifying junction, with a current significantly higher under forward bias than under reverse bias. The magnitude of the measured current is quite high, with μA level currents measured at –100 V. This is two orders of magnitude higher than what is typically expected from CsPbBr₃. There also appears to be substantial ionic mobility measured, as seen by the opening of the hysteresis in both the forward and reverse bias. Conversely, the CsPbBr₃ crystal cut parallel to the growth direction features I–V characteristics that are much more promising. Similar to previous investigations, 10 nA dark currents are measured at –100 V. A rectifying junction appears to have formed, with a forward bias $\sim 4\times$ higher than the reverse bias, though this I–V characteristic does not have a clear knee voltage to measure a Schottky barrier height, rather a sharp increase in the measured current at ~ 0 V. This may be due to the presence of the SiO₂ layer which may build up charge and discharge over the course of the measurement. Forward bias appears to have some degree of ionic mobility with the presence of a hysteresis loop; however, reverse bias conditions eliminate this with no hysteresis observed. This may be due to which ions are mobile in this crystal system, with negatively charged ions (Br[–]) being more mobile and able to drift under positive bias or may be associated with the electrode/passivation structure being more effective at blocking the collection of ionic-induced current measurements. Through comparing the I–V characteristics of these crystal structures, it is clear that cutting the CsPbBr₃ parallel to the growth direction is advantageous for lowering measured dark currents.

Current–time characteristics were measured to observe the variance of dark current over time. These measurements were conducted at a constant bias of –100 V for 10 min. The sample cut perpendicular to the growth direction begins with a fairly high measured dark current (~ -450 nA), which then asymptotically decreases over the measurement period, and begins to level out (~ 50 nA). This is in stark comparison to the CsPbBr₃ crystal cut parallel to the growth direction, which has almost no change in the measured dark current throughout the duration of the measurement. In this study, both CsPbBr₃ crystals were coated with 10 nm of SiO₂ with identical contact structures, meaning that the degree of surface ion mobility is likely similar between the two crystals. As such, the change in current–time characteristics must be associated with the bulk of the crystal. Recall that the perpendicular-cut sample has more crystallographic boundaries within the bulk, particularly twin boundaries. These boundaries likely serve as fast conduction

pathways for both electrons/holes and ions. This is observed under the standard I–V characteristics, where both large dark currents and hysteresis are observed. In the current–time characteristics, changes in the measured current are likely associated with varying ionic contributions during the measurement. During the 10-min measurement window, ions are successfully depleted from the bulk resulting in a lowering and stabilizing dark current measurement. Comparing this to the parallel-cut sample, there are not sufficient pathways (twin/orientation boundaries) to promote bulk ion diffusion. This, combined with the SiO₂ coating which suppresses surface ion movement, results in a current–time characteristic which is not strongly influenced by moving ions and stays constant throughout (Figure 11). Clearly, crystallographic orientation has a significant effect on both the conductivity of the device and the temporal stability.

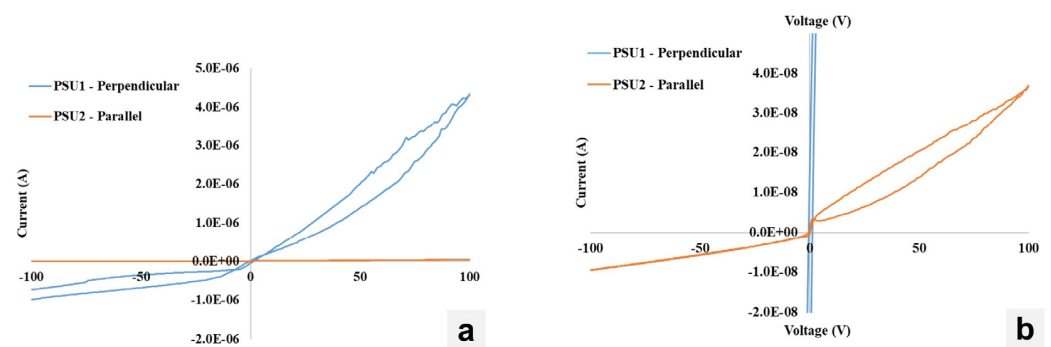


Figure 10. (a) I–V characteristics of single CsPbBr₃ crystals cut perpendicular and parallel to the growth direction. (b) Zoomed-in view to resolve the parallel growth direction I–V characteristics.

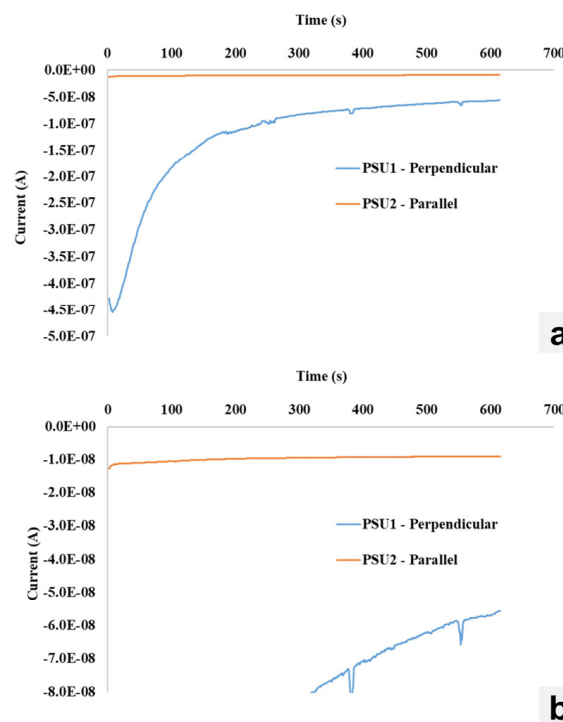


Figure 11. (a) Current–time characteristics measured at a constant -100 V bias for CsPbBr₃ samples cut perpendicular and parallel to the growth direction. (b) Zoomed-in view to resolve the parallel direction.

Table 1 shows a summary of the CsPbBr₃ bulk resistivity values measured with different planar device configurations.

Table 1. Bulk resistivity values measured with different contact configurations.

Sample Contacts	ρ fwd ($\Omega \cdot \text{cm}$)	ρ rev ($\Omega \cdot \text{cm}$)
Bi–Au	$2.5\text{--}3 \times 10^9$	$1.8\text{--}5.9 \times 10^8$
Au–Au	9.5×10^8	2.8×10^9
InGa–Au	2×10^9	
In–Au	2.5×10^9	10^{10}

3.2. Photocurrent Spectroscopy and Optical Measurements

Figure 12a shows the photocurrent spectrum of the CsPbBr₃ sample pictured in Figure 7a held at a constant bias of +300 V, while Figure 12b shows the photocurrent spectrum at –300 V. Both spectra show a peak at 550 nm or 2.25 eV, which is within the bandgap energy range for CsPbBr₃. In order to estimate the mobility–lifetime product ($\mu\tau$), the sample was illuminated with a beam of light of 525 nm wavelength that was just below the wavelength of the peak of the photocurrents. At this wavelength, the light was highly absorbed by the sample close to the surface of illumination, and all of the charge carriers generated could travel through the entire thickness of the sample. The choice of the wavelength value is based on the absorption spectrum and photocurrent spectra as shown in Figure 12c.

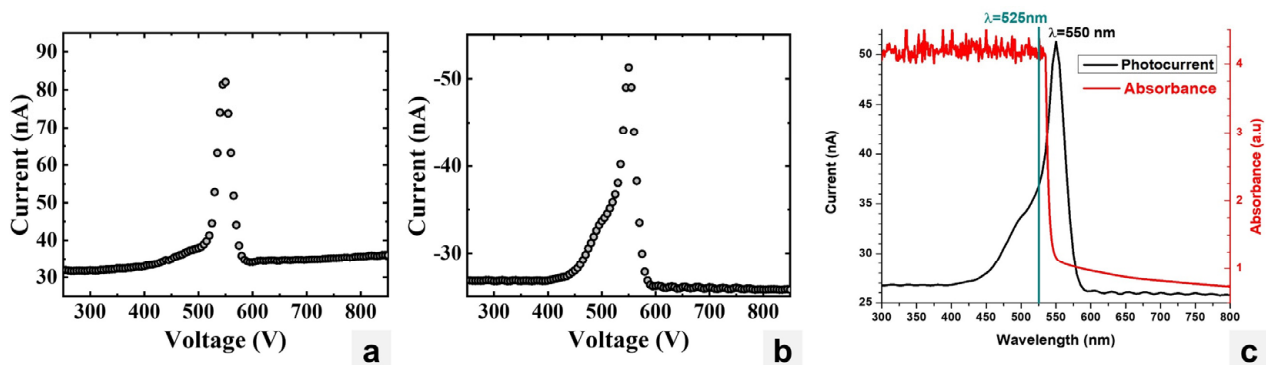


Figure 12. (a) Photocurrent spectrum for CsPbBr₃ at +300 V. (b) Photocurrent spectrum for CsPbBr₃ at –300 V. (c) Absorbance spectrum of CsPbBr₃ with 525 nm light illumination.

Figure 13 shows the photoluminescence and photoluminescence (PL) lifetime measurements on the CsPbBr₃ and CsPb(Br,I)₃ devices fabricated at Northwestern. The photoluminescence spectrum of CsPbBr₃ in Figure 13a shows a broad spectrum with a peak around 529 nm or 2.34 eV, while the photoluminescence spectrum of CsPb(Br,I)₃ in Figure 13b had a peak around 536 nm or 2.31 eV. The PL lifetime for CsPbBr₃ was measured at 6 ns (Figure 13c), while the lifetime for CsPb(Br,I)₃ was measured at 2 ns (Figure 13d). The low lifetime values, which are about 1 to 2 orders of magnitude lower than expected [20], may be caused by impurities and defects. The broad peaks in the room-temperature photoluminescence spectra are an indication of the complex structure of the exciton levels in this class of materials.

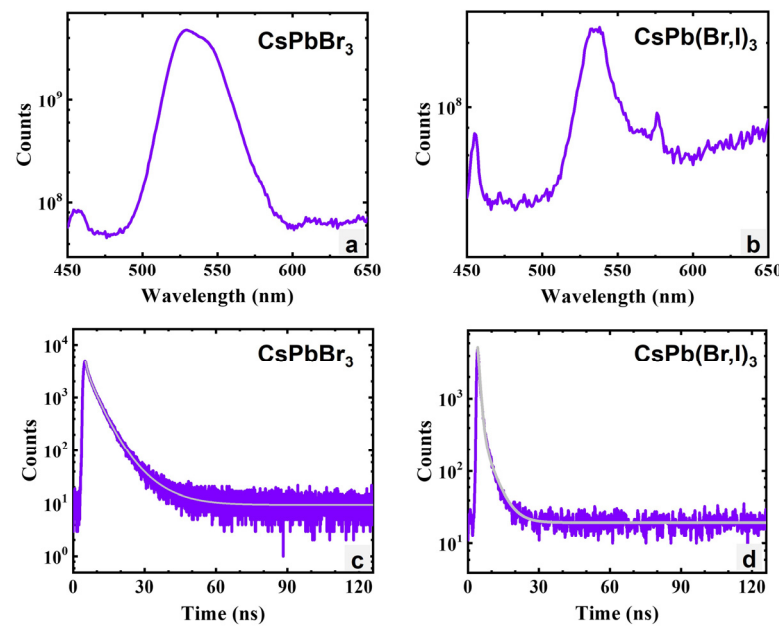


Figure 13. (a) Photoluminescence spectrum of CsPbBr₃. (b) Photoluminescence spectrum of CsPb(Br,I)₃. (c) PL lifetime of CsPbBr₃. (d) PL decay curve of CsPb(Br,I)₃.

3.3. Estimation of the Mobility–Lifetime Product ($\mu\tau$)

Figure 14a shows the graph of current as a function of applied reverse bias from 0 to -500 V with and without the 525 nm illumination (Figure 12c). The photocurrent curve was obtained by subtracting the dark current (measured without illumination) from the current measured with illumination. The light-generated charge carriers' contribution was determined by fitting the photocurrent curve using the Hecht equation defined as the following:

$$\eta(V) = \mu\tau \cdot \frac{V}{L^2} \left(1 - \exp\left(-\frac{L^2}{\mu\tau V}\right) \right) \quad (3)$$

where η is the charge collection efficiency, μ is the mobility (in $\text{cm}^2/\text{V}\cdot\text{s}$), τ is the lifetime (in s), L is the detector thickness (in cm), and V is the applied bias (in volts). Figure 14b shows the photocurrent data fitted with the Hecht equation, resulting in a calculated $\mu\tau$ of $2.8 \times 10^{-4} \text{ cm}^2/\text{V}$.

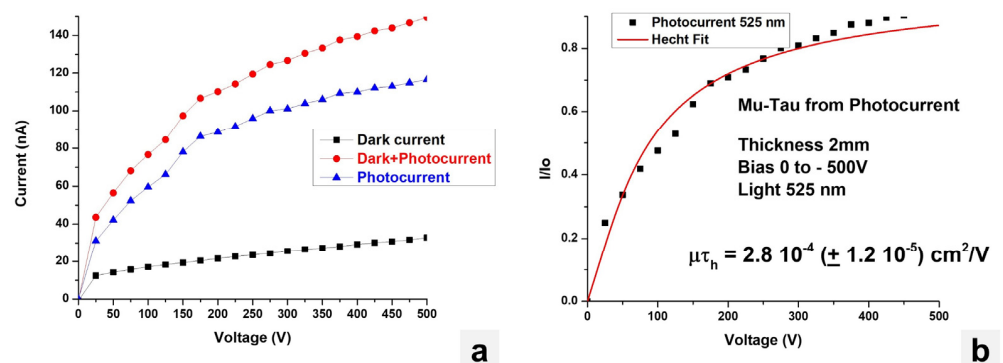


Figure 14. (a) Current data measured with and without illumination. (b) Photocurrent data fitted with the Hecht equation.

Another commonly used method to determine the $\mu\tau$ product is to irradiate the device with alpha particles and determine the peak centroid as the function of the bias voltage. Figure 15a shows the ²⁴¹Am alpha spectra as a function of bias and measured

by the CsPbBr₃ device shown in Figure 7a. Figure 15b shows the graph of the peak centroid as the function of the bias voltage. Fitting the data with the Hecht equation, $\mu\tau$ of $2.8 \times 10^{-5} \text{ cm}^2/\text{V}$ was estimated.

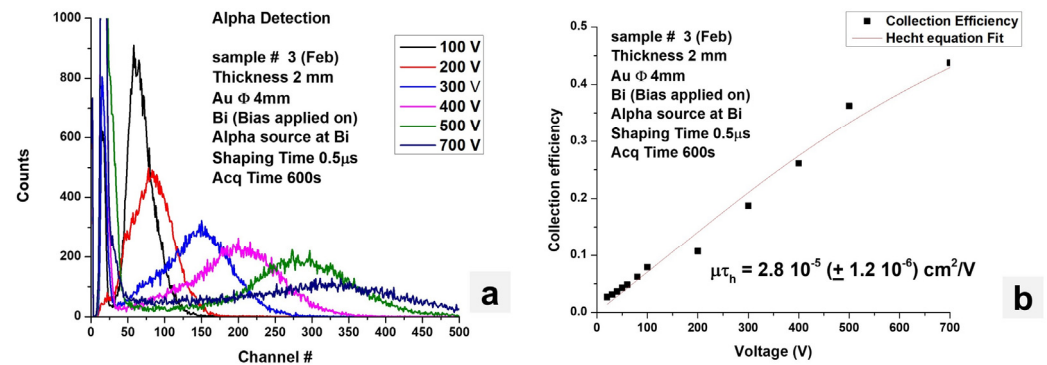


Figure 15. (a) Alpha spectra collected by CsPbBr₃. (b) Peak centroid vs. bias voltage data fitted with Hecht's equation.

4. Conclusions

Using the zone-refining technique, clear and transparent crystal boules were obtained, compared to the unpurified material crystal boules. Crystals up to 1 inch in diameter were grown and cut into wafers with different orientations to evaluate the surface fabrication and contact deposition. Using CMP (chemical–mechanical polishing) techniques, a visibly smooth surface was obtained compared to only using SiC paper. The I–V characteristics showed a low dark current but displayed some noise. Leaving a sample under bias was used to increase the performance, but the sample still displayed noise after too much time under bias. It was observed that cutting the crystal parallel to growth rather than perpendicular resulted in a lower starting dark current. Samples cut perpendicular to crystal growth are believed to have more crystallographic boundaries such as twin boundaries which would explain the discrepancy in the I–V characteristics of the samples. The absorption spectrum of CsPbBr₃ showed that at 525 nm, light was highly absorbed close to the surface of the sample meaning that the excited charge carrier would travel through the entirety of the sample. We have succeeded in demonstrating the preparation of a high bulk resistivity up to $3.0 \times 10^9 \Omega\text{-cm}$ and wafers with surface resistivity values of $1.3 \times 10^{11} \Omega/\square$ which are the pre-requisites in the fabrication of large-volume nuclear radiation detectors. Low lifetime values were also observed during photocurrent decay measurements, which could be a result of impurities and defects in the crystal. The different distinct samples and their respective results will allow improvements to the crystal itself as well as a different approach to the fabrication of samples for future studies and experiments.

Author Contributions: Conceptualization, R.H.; methodology, R.H., L.M., E.A., V.B., H.P., A.B., J.S., A.P., F.D.F., A.K., K.S.B., J.R., and D.E.W.; validation, R.H. and E.A.; formal analysis, L.M. and E.A.; investigation, R.H., L.M., E.A., V.B., H.P., A.B., J.S., A.P., F.D.F., A.K., K.S.B., and J.R.; resources, R.H., A.B., and D.E.W.; data curation, R.H. and E.A.; writing—original draft preparation, R.H., L.M., E.A., A.P., F.D.F., A.K., K.S.B., A.K., and J.R.; writing—review and editing, R.H., L.M., E.A., and A.B.; visualization, R.H., L.M., E.A., A.K., K.S.B., and J.R.; supervision, R.H. and D.E.W.; project administration, R.H. and D.E.W.; funding acquisition, R.H. and D.E.W. All authors have read and agreed to the published version of the manuscript.

Funding: This work was supported in part by the Defense Threat Reduction Agency Interaction of Ionizing Radiation in Materials University Research Alliance (DTRA IIRM URA) under Cooperative Agreement No. HDTRA1-20-2-0002, the U.S. Air Force Office of Scientific Research Grant No. FA9550-22-1-0343, and the U.S. National Science Foundation Grant No. HRD-2112556.

Institutional Review Board Statement: Not applicable.

Informed Consent Statement: Not applicable.

Data Availability Statement: Contact Corresponding Author for more information.

Acknowledgments: This work was supported in part by the Defense Threat Reduction Agency Interaction of Ionizing Radiation in Materials University Research Alliance (DTRA IIRM URA) under Cooperative Agreement No. HDTRA1-20-2-0002, the U.S. Air Force Office of Scientific Research Grant No. FA9550-22-1-0343, and the U.S. National Science Foundation Grant No. HRD-2112556.

Conflicts of Interest: Author A. Kargar was employed by the company Radiation Monitoring Devices, Inc. The remaining authors declare that the research was conducted in the absence of any commercial or financial relationships that could be construed as a potential conflict of interest.

References

1. Schlesinger, T.E.; Toney, J.E.; Yoon, H.; Lee, E.Y.; Brunett, B.A.; Franks, L.; James, R.B. Cadmium zinc telluride and its use as a nuclear radiation detector material. *Mater. Sci. Eng. R Rep.* **2001**, *32*, 103–189. [[CrossRef](#)]
2. Gehrels, N.; Chincarini, G.; Giommi, P.E.; Mason, K.O.; Nousek, J.A.; Wells, A.A.; Zhang, W.W. The Swift Gamma-Ray Burst Mission. *Astrophys. J.* **2004**, *611*, 1005. [[CrossRef](#)]
3. Iniewski, K. CZT detector technology for medical imaging. *J. Instrum.* **2014**, *9*, C11001. [[CrossRef](#)]
4. Atsuro, S.; Wataru, T.; Takafumi, I.; Katsutoshi, T.; Yuichi, M.; Yuichiro, U.; Keiji, K.; Naoki, K.; Tohru, S.; Nagara, T. High-sensitivity brain SPECT system using cadmium telluride (CdTe) semiconductor detector and 4-pixel matched collimator. *Phys. Med. Biol.* **2013**, *58*, 7715.
5. Khodyuk, I.V.; Dorenbos, P. Trends and patterns of scintillator nonproportionality. *IEEE Trans. Nucl. Sci.* **2012**, *59*, 3320–3331. [[CrossRef](#)]
6. Burger, A.; Nason, D.; Franks, L. Mercuric iodide in prospective. *J. Cryst. Growth* **2013**, *379*, 3–6. [[CrossRef](#)]
7. Alam, D. Recent progress in CdZnTe based room temperature detectors for nuclear radiation monitoring. *Prog. Nucl. Energy* **2021**, *140*, 103918. [[CrossRef](#)]
8. Koslov, V. *TlBr Raw Material Purification, Crystal Growth, Annealing, Detector Fabrication and Characterization for Gamma-Ray Detector Applications*; University of Helsinki: Helsinki, Finland, 2010.
9. Stoumpos, C.C.; Malliakas, C.D.; Peters, J.A.; Liu, Z.; Sebastian, M.; Im, J.; Chasapis, T.C.; Wibowo, A.C.; Chung, D.Y.; Freeman, A.J.; et al. Crystal Growth of the Perovskite Semiconductor CsPbBr₃: A New Material for High-Energy Radiation Detection. *Cryst. Growth Des.* **2013**, *13*, 2722–2727. [[CrossRef](#)]
10. Dirin, D.N.; Cherniukh, I.; Yakunin, S.; Shynkarenko, Y.; Kovalenko, M.V. Solution-Grown CsPbBr₃ Perovskite Single Crystals for Photon Detection. *Chem. Mater.* **2016**, *28*, 8470–8474. [[CrossRef](#)] [[PubMed](#)]
11. He, Y.; Matei, L.; Jung, H.J.; McCall, K.M.; Chen, M.; Stoumpos, C.C.; Liu, Z.; Chung, D.Y.; Wessels, B.W.; et al. High Spectral Resolution of Gamma-rays at Room Temperature by Perovskite CsPbBr₃ Single Crystals. *Nat. Commun.* **2018**, *9*, 1609. [[CrossRef](#)] [[PubMed](#)]
12. Pan, L.; Feng, Y.; Huang, J.; Cao, L.R. Comparison of Zr, Bi, Ti, and Ga as metal contacts inorganic perovskite CsPbBr₃ gamma-ray detector. *IEEE Trans. Nucl. Sci.* **2020**, *67*, 2255–2262. [[CrossRef](#)]
13. He, Y.; Liu, Z.; McCall, K.M.; Lin, W.; Chung, D.Y.; Wessels, B.W.; Kanatzidis, M.G. Perovskite CsPbBr₃ single crystal detector for alpha particle spectroscopy. *Nucl. Instrum. Methods A* **2019**, *922*, 217–221. [[CrossRef](#)]
14. Zhang, X.; Bai, R.; Fu, Y.; Hao, Y.; Peng, X.; Wang, J.; Xu, Y. High energy resolution CsPbBr₃ alpha particle detector with a full-customized readout application specific integrated circuit. *Nat. Commun.* **2024**, *15*, 6333. [[CrossRef](#)] [[PubMed](#)]
15. Pan, L.; Feng, Y.; Kandlakunta, P.; Huang, J.; Cao, L.R. Performance of Perovskite CsPbBr₃ Single Crystal Detector for Gamma-Ray Detection. *IEEE Trans. Nucl. Sci.* **2020**, *67*, 443–449. [[CrossRef](#)]
16. Feng, Y.; Pan, L.; Wei, H.; Liu, Y.; Ni, Z.; Zhao, J.; Rudd, P.N.; Cao, L.R.; Huang, J. Low Defects Density CsPbBr₃ Single Crystals Grown by an Additive Assisted Method for Gamma-Ray Detection. *J. Mater. Chem. C* **2020**, *8*, 11360–11368. [[CrossRef](#)]
17. Pfann, W.G. *Zone Melting*; John Wiley & Sons: New York, NY, USA, 1966.
18. Feigelson, R.S. Crystal Growth Through the Ages: A Historical Perspective. In *The Handbook of Crystal Growth*, 2nd ed.; Elsevier: Amsterdam, The Netherlands, 2015; Volume 1A, pp. 1–83.
19. Toufanian, R.; Swain, S.; Becla, P.; Motakef, S.; Datta, A. Cesium Lead Bromide Semiconductor Radiation Detectors: Crystal Growth, Detector Performance and Polarization. *J. Mater. Chem. C* **2022**, *10*, 12708–12714. [[CrossRef](#)]
20. Pan, L.; Pandey, I.R.; Miceli, A.; Klepov, V.V.; Chung, D.Y.; Kanatzidis, M.G. Perovskite CsPbBr₃ Single-Crystal Detector Operating at 10¹⁰ Photons S⁻¹ Mm⁻² for Ultra-High Flux X-Ray Detection. *Adv. Opt. Mater.* **2023**, *11*, 2202946. [[CrossRef](#)]

Disclaimer/Publisher's Note: The statements, opinions and data contained in all publications are solely those of the individual author(s) and contributor(s) and not of MDPI and/or the editor(s). MDPI and/or the editor(s) disclaim responsibility for any injury to people or property resulting from any ideas, methods, instructions or products referred to in the content.